Electronic Supplementary Information (ESI)

Core-Multi-Shell Design: Unlocking Multimodal Capabilities in Lanthanide-based Nanoparticles as Upconverting, T_2-Weighted MRI and CT Probes

Nan Liu,[a] Christian Homann,[a] Samuel Morfin,[b] Meghana Kesanakurti,[a] Nicholas D. Calvert,[a,c] Adam J. Shuhendler,[a,c,d] Tom Al,[b] and Eva Hemmer*[a]

[a] Department of Chemistry and Biomolecular Sciences, University of Ottawa, 10 Marie-Curie Private, Ottawa (ON) K1N 6N5, Canada.

[b] University of Ottawa Heart Institute, Ottawa (ON), Canada.

[c] Department of Earth and Environmental Sciences, University of Ottawa, Ottawa (ON), Canada.

[d] Department of Biology, University of Ottawa, Ottawa (ON), Canada.

* Corresponding Author E-mail: ehemmer@uottawa.ca

Table of Contents

1. Additional Experimental Details

Table S1. Overview of the compositions and dimensions of the core, CS, and CSS NPs used in this study. Green shaded samples were used to study the effect of inner shell thickness on UC. Blue shaded samples were used to study the effect of outer shell thickness on MRI and CT performance. Sample ^{4nm}Dy-CSS^{3nm} was used in both studies.

Sample Code	$NaGdF_4$:Yb,Er Core Size (nm)	$NaGdF_4$ Inner Shell Thickness (nm)	$NaDyF_4$ Outer Shell Thickness (nm)	Overall Particle Size (nm)	Surface Chemistry	Investigated Performance
Dy-CS	5.3 ± 0.5	-	3.4	12.1 ± 1.0	oleate	UC
^{3nm}CS	5.3 ± 0.5	3.0	-	11.3 ± 0.3	oleate	UC
^{3nm}Dy-CSS^{3nm}			3.0	17.3 ± 1.3		
^{4nm}CS	5.0 ± 0.2	3.9	-	12.8 ± 1.0	oleate	UC
^{4nm}Dy-CSS^{3nm}			2.7	18.1 ± 1.1	oleate, citrate	
^{6nm}CS	5.7 ± 0.2	5.7	-	17.0 ± 1.1	oleate	UC, MRI
^{6nm}Dy-CSS^{3nm}			2.5	22.0 ± 1.3	oleate, citrate	
^{4nm}CS	5.4 ± 0.2	4.4	-	14.2 ± 0.9	oleate	UC
^{4nm}Dy-CSS^{1nm}			1.3	16.9 ± 1.0	oleate, citrate	UC, MRI, CT
^{4nm}CS	5.0 ± 0.2	3.9	-	12.8 ± 1.0	oleate	UC
^{4nm}Dy-CSS^{3nm}			2.7	18.1 ± 1.1	oleate, citrate	UC, MRI, CT
^{4nm}CS	5.1 ± 0.3	4.3	-	13.8 ± 1.0	oleate	UC
^{4nm}Dy-CSS^{4nm}			4.0	21.9 ± 1.3	oleate, citrate	UC, MRI, CT

Core/shell (CS) and core/shell/shell (CSS) NPs were synthesized using a modified version of the microwave-assisted approach previously published by our group.[1] For the synthesis of the CS NPs, core NPs act as seeds for the epitaxial growth of the undoped $NaGdF_4$ shell. Herein, adjustment of the ratio between the core NP seeds and the shell precursor in the reaction mixture was found to be key. Decreasing the number of core NPs, while keeping the amount of shell precursor constant allowed to tune the thickness of the undoped $NaGdF_4$ shell on the Er^{3+}/Yb^{3+}-co-doped core from ca. 3 to 4 and 6 nm (^{3nm}CS, ^{4nm}CS, and ^{6nm}CS), respectively (Figure S1A and Figure 1). Similarly, during the synthesis of CSS Dy-NPs, the thickness of the outer $NaDyF_4$ shell could be tuned by controlling the ratio of CS NP seeds and the Dy-TFA precursor in the reaction mixture from ca. 1 to 3 and 4 nm (^{4nm}Dy-CSS^{1nm}, ^{4nm}Dy-CSS^{3nm}, and ^{4nm}Dy-CSS^{4nm}), respectively (right panel in Figure S1A and Figure S9).

However, when the ratio between core NPs and shell precursor in the reaction mixture dropped below a critical value (*i.e.*, a mass of core NPs of less than 30 mg), flower-like NPs were formed. The relatively high concentration of shell precursor is proposed to lead to the nucleation and subsequent growth of individual undoped $NaGdF_4$ NPs at the surface of the core NPs.[2] This ultimately results in heterogeneous structures that resemble flower petals (Figure S1B).

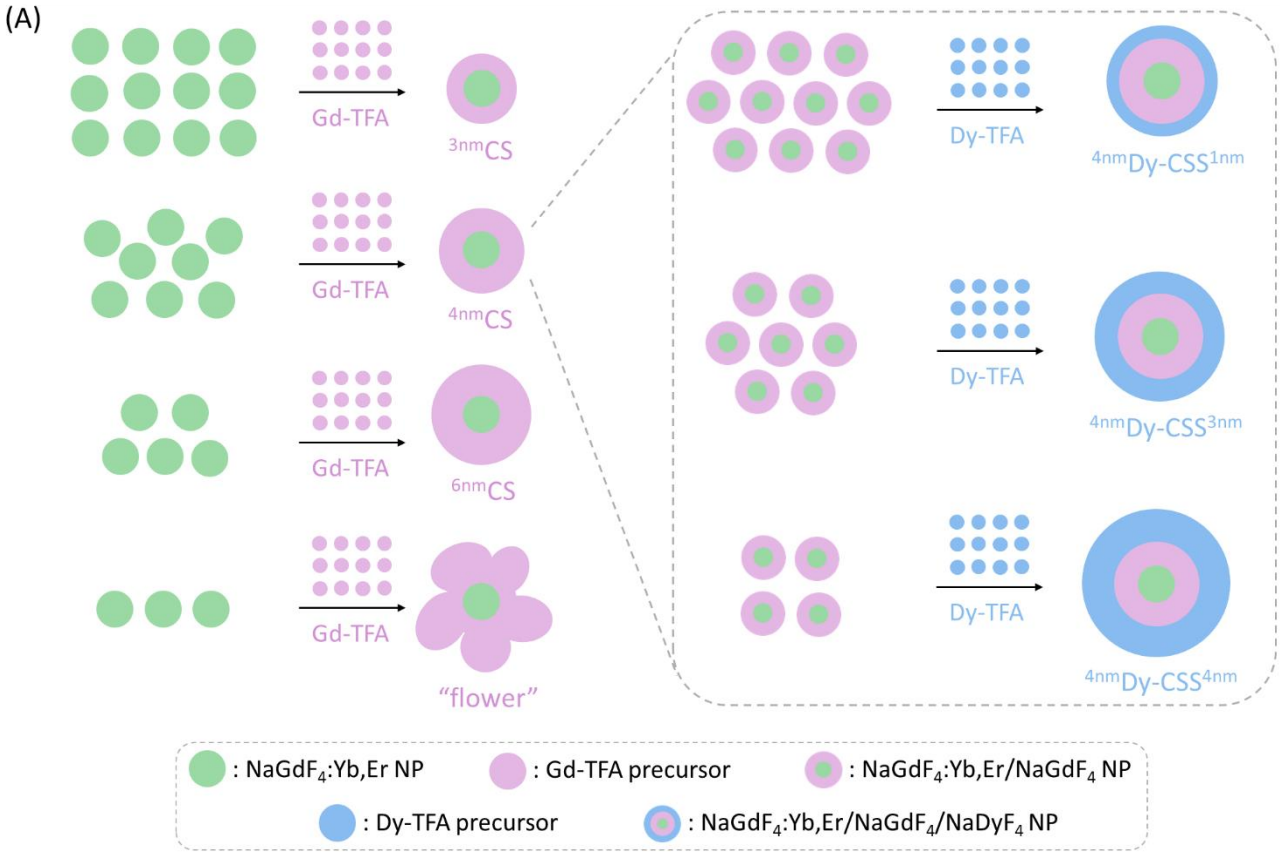

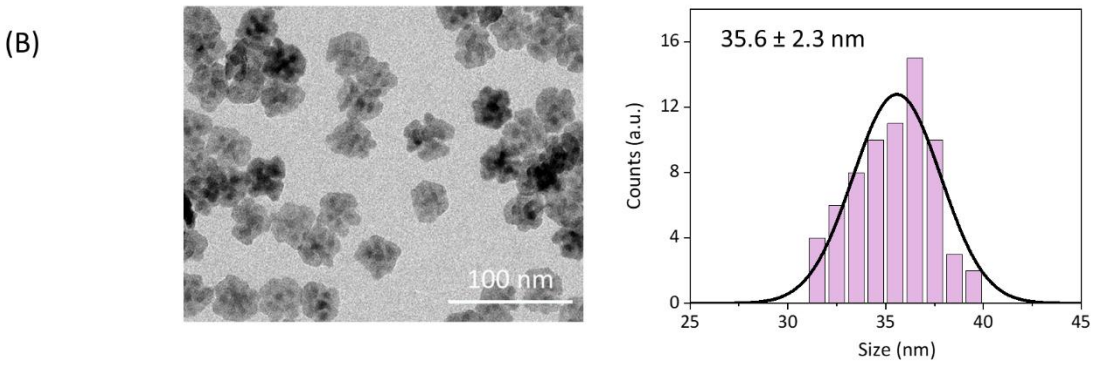

Figure S1. (A) Schematic representation of microwave-assisted shell thickness control in core/shell and core/shell/shell Dy-NP architectures. (B) TEM image of "flower-like" CS NPs and their corresponding size distribution.

2. Additional Structural Analysis by XRD and TEM

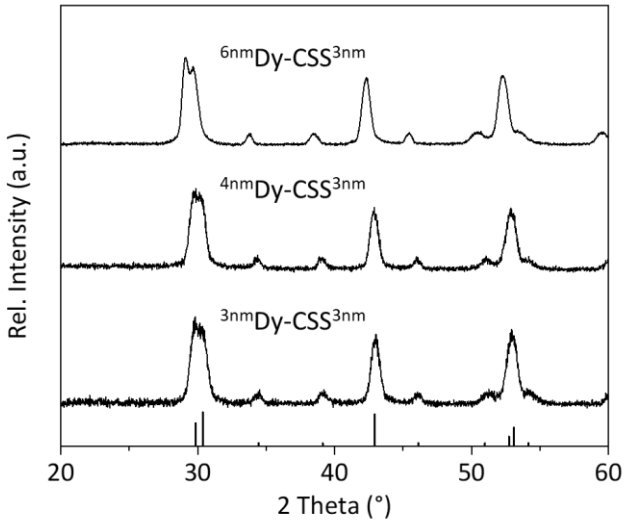

Figure S2. XRD patterns of oleate (OA)-capped core/shell/shell β-$NaGdF_4$:Yb,Er/$NaGdF_4$/$NaDyF_4$ (Dy-CSS) with different inner shell thicknesses of 3.0 nm (^{3nm}Dy-CSS^{3nm}), 3.9 nm (^{4nm}Dy-CSS^{3nm}), and 5.7 nm (^{6nm}Dy-CSS^{3nm}), respectively. Reference: β-$NaGdF_4$, PDF card [01-080-8787].

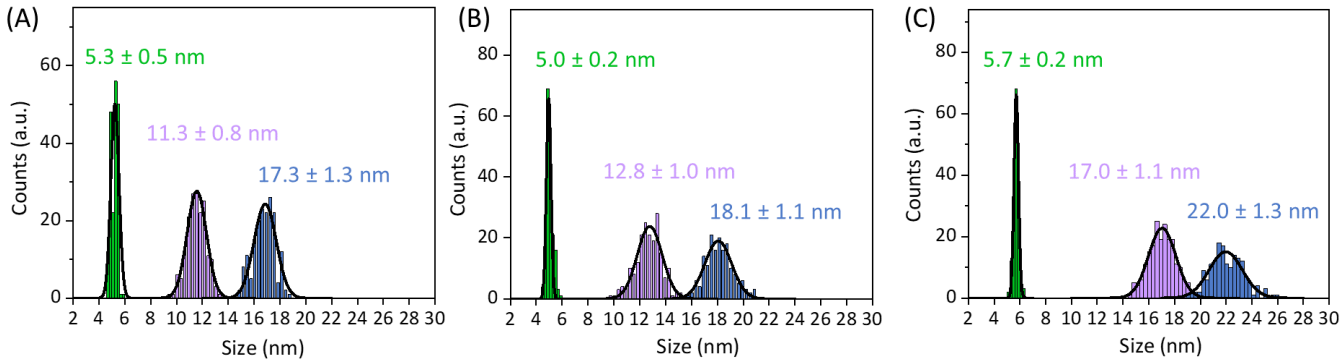

Figure S3. Size distributions of (A) ^{3nm}Dy-CSS^{3nm}, (B) ^{4nm}Dy-CSS^{3nm}, as well as (C) ^{6nm}Dy-CSS^{3nm} NPs and their corresponding CS (^{3nm}CS, ^{4nm}CS, ^{6nm}CS) and core NPs, demonstrating the varying thickness of the inner shell, while keeping core size and outer shell thickness constant.

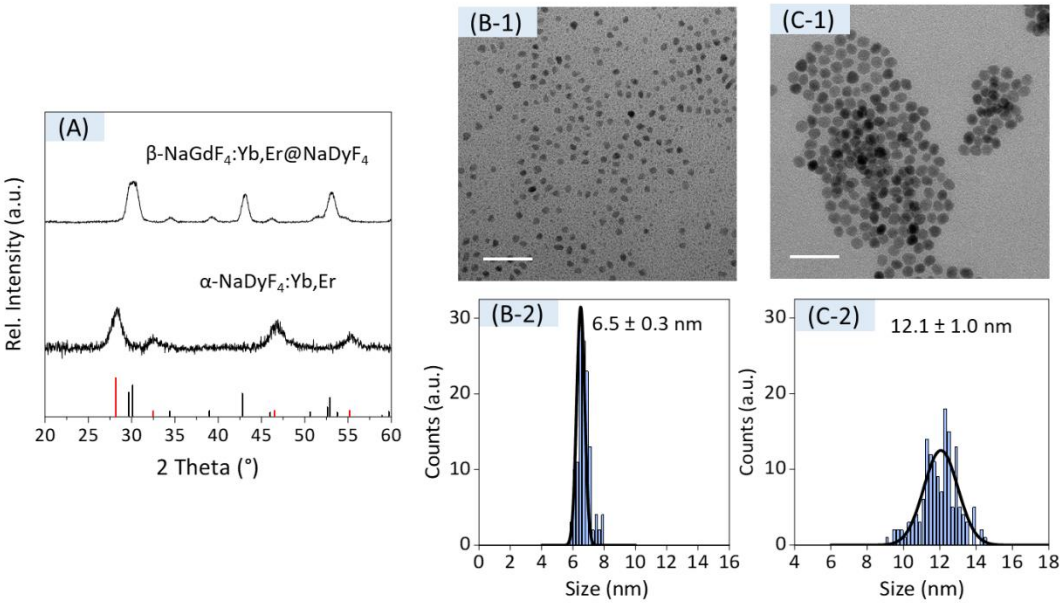

Figure S4. (A) XRD patterns of OA-capped α-$NaDyF_4$:Yb,Er core and β-$NaGdF_4$:Yb,Er/$NaDyF_4$ (Dy-CS) core-shell NPs. References: red line – α-$NaDyF_4$, PDF card [00-027-0697]; black line – β-$NaGdF_4$, PDF card [01-080-8787]. (B and C) (1) TEM images and (2) their corresponding size distributions of OA-capped (B) α-$NaDyF_4$:Yb,Er and (C) β-$NaGdF_4$:Yb,Er/$NaDyF_4$ NPs. Scale bars: 50 nm. Note that β-$NaDyF_4$:Yb,Er is not accessible *via* our microwave-assisted synthesis.[3] Therefore, α-$NaDyF_4$:Yb,Er was used as a similar-sized reference core sample.

3. Additional Optical Characterization of OA-capped NPs

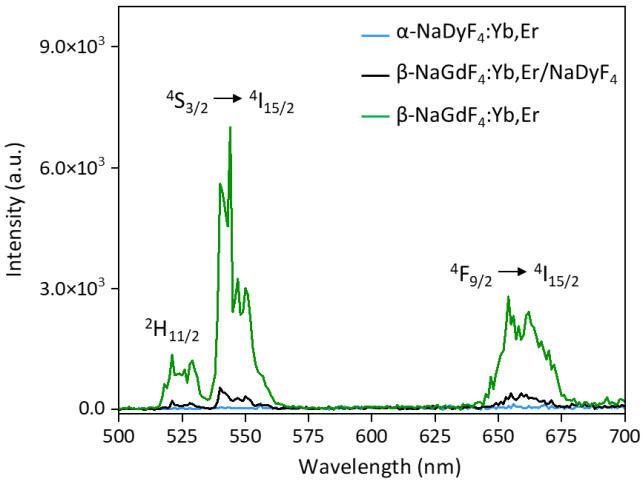

Figure S5. UC spectra of OA-capped α-$NaDyF_4$:Yb,Er, β-$NaGdF_4$:Yb,Er, and β-$NaGdF_4$:Yb,Er/$NaDyF_4$ CS NPs. All spectra were obtained under 980 nm laser excitation. Power density = 6.0 W/cm^2, [NP] = 5 mg/mL in toluene.

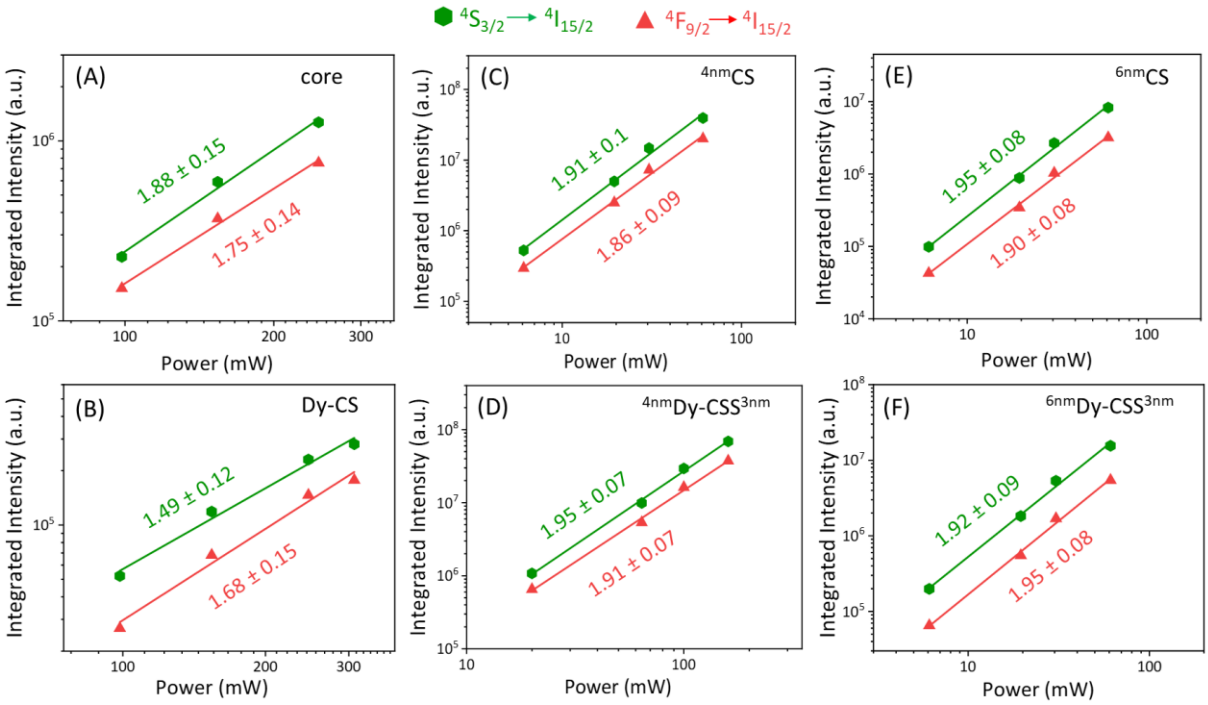

Figure S6. Integrated $^4S_{3/2} \rightarrow {}^4I_{15/2}$ and $^4F_{9/2} \rightarrow {}^4I_{15/2}$ Er^{3+} emission intensities *versus* 980 nm excitation power for OA-capped (A) β-$NaGdF_4$:Yb,Er (core), (B) Dy-CS, (C) ^{4nm}CS, (D) ^{4nm}Dy-CSS^{3nm}, (E) ^{6nm}CS, and (F) ^{6nm}Dy-CSS^{3nm} NPs.

Regardless of the architecture of the NPs, the slopes of the fitted curves of the log-log power plots (which reflect the number of photons involved in the UC process[4]) were larger than 1 for both the green ($^4S_{3/2} \rightarrow {}^4I_{15/2}$) and red ($^4F_{9/2} \rightarrow {}^4I1_{5/2}$) Er^{3+} upconversion emissions (Figure S6). Thus, a 2-photon process took place, as expected for the Yb^{3+}/Er^{3+} upconversion ion pair. Nonetheless, the presence of Dy was found to have an influence on the UC process. Interestingly, the addition of a $NaDyF_4$ shell on the Er^{3+}/Yb^{3+}-doped core lowered the slope values of the double logarithmic power plots from 1.88 to 1.49 and 1.75 to 1.68 for the green and red emissions, respectively (Figure S6A-B). This decrease in the slope values indicated a

perturbation of the classical UC process for which a slope close to 2 would be expected, along with energy transfer from Er^{3+}/Yb^{3+} to Dy^{3+} as a competing process. Moreover, this observation agrees with the reduced Er^{3+} UC emission (Figure S5) and shortened lifetime of the Yb^{3+} excited state (Figure 2C). When adding a 4 nm undoped $NaGdF_4$ shell on the Er^{3+}/Yb^{3+}-doped core (^{4nm}CS NPs), the values slightly increased to 1.91 and 1.86 for the green and red emission (Figure 6C), approaching the theoretical value of 2. This increase was ascribed to the prevention of surface quenching *via* inner shelling. Upon further growth of a $NaDyF_4$ outer shell (^{4nm}Dy-CSS^{3nm} NPs), minor additional increase of the slope values to 1.95 and 1.91 was observed (Figure S6D). This might indicate that the energy transfer process from Er^{3+}/Yb^{3+} to Dy^{3+} was not dominant anymore but that recovery of classical 2-photon UC process took place. The same trend was observed for ^{6nm}CS NPs (green: 1.95, red: 1.90) and ^{6nm}Dy-CSS^{3nm} NPs (green: 1.92, red: 1.95) (Figure S6E/F).

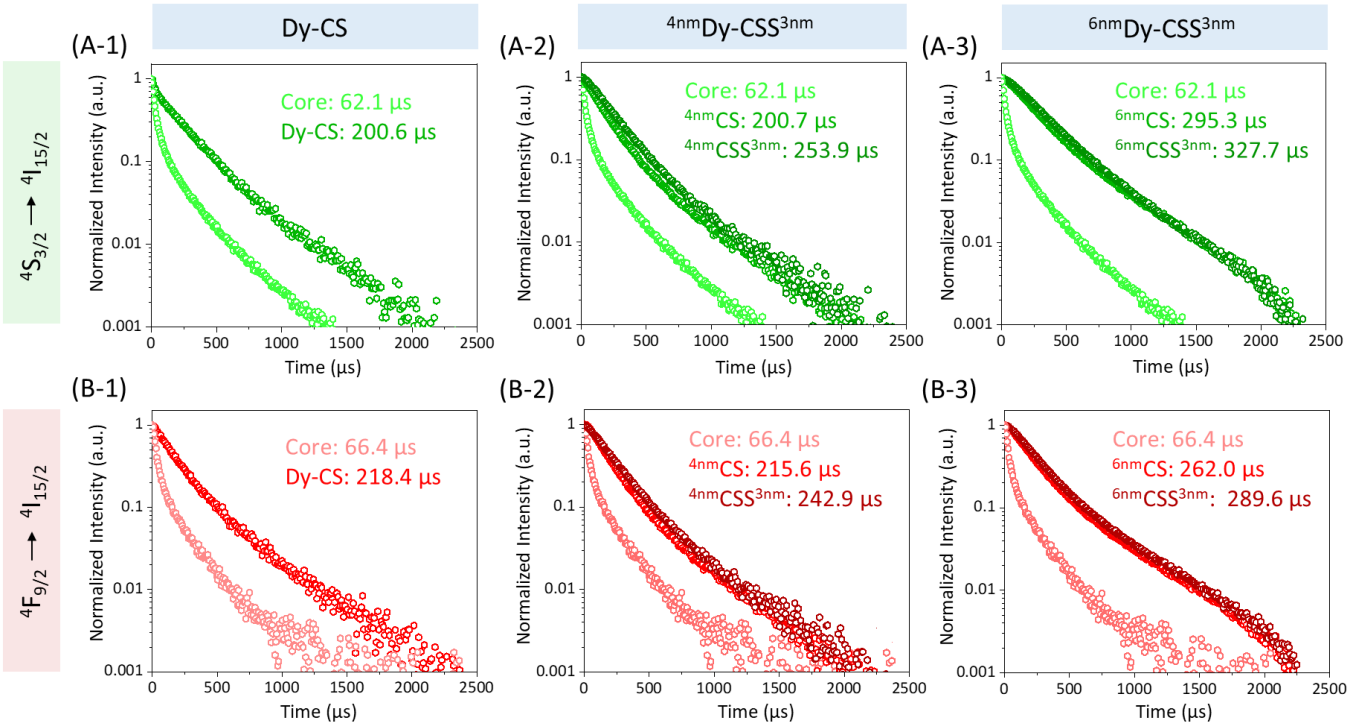

Figure S7. Luminescence decay curves of the (A) $^4S_{3/2} \rightarrow {}^4I_{15/2}$ (540 nm) and (B) $^4F_{9/2} \rightarrow {}^4I_{15/2}$ (650 nm) Er^{3+} transitions for (1) Dy-CS, (2) ^{4nm}Dy-CSS^{3nm}, and (3) ^{6nm}Dy-CSS^{3nm} NPs and their corresponding core and CS NPs in toluene. λ_{ex} = 980 nm.

Fluorescence decay curves and the corresponding lifetimes of the green and red Er^{3+} emissions at 540 nm ($^4S_{3/2} \rightarrow {}^4I_{15/2}$) and 650 nm ($^4F_{9/2} \rightarrow {}^4I_{15/2}$) under 980 nm excitation are shown in Figure S7. As expected, the small core NPs exhibited relatively short lifetimes for the green (62.1 µs) and red (66.4 µs) emissions due to surface quenching. The slightly longer lifetime for the red emission is in agreement with previous studies.[1, 5] Growth of a passivating shell is expected to increase the lifetimes of the green and red emissions, along with increased photoluminescence intensities, due to reduced surface quenching. In line, lifetimes prolonged to more than 200 µs upon growth of an undoped $NaGdF_4$ shell (^{4nm}CS and ^{6nm}CS NPs, Figure S7A/B-2/3), whereas increased shell thickness resulted in longer lifetimes.

Shelling of an Er^{3+}/Yb^{3+}-doped $NaGdF_4$ core with $NaDyF_4$ resulted in severe loss of UC emission (Figure S5). Yet, noteworthy, the Er^{3+} lifetime values of Dy-CS NPs (Figure S7A/B-1) were comparable to those obtained for ^{4nm}CS and ^{6nm}CS NPs with a $NaGdF_4$ shell (green emission: 200.6 µs, red emission: 218.4 µs). This indicated that Dy^{3+} ions in the shell do not significantly contribute to UC emission loss *via* non-radiative

depopulation of the excited Er^{3+} levels. Rather, both shell types – $NaGdF_4$ and $NaDyF_4$ – protect the Er^{3+} emitters from surface quenching, leading to similar lifetimes. To recall, lifetime measurements of the Yb^{3+} emission provided evidence for energy transfer from Yb^{3+} in the core to Dy^{3+} ions in the shell, depopulating the excited Yb^{3+} state and hence, hampering efficient UC of Er^{3+} to the ion's emitting levels. Thus, while radiative decay of Er^{3+} ions once excited to the green- and red-emitting levels took place upon shelling with $NaDyF_4$, the Yb^{3+}-sensitized population of these emitting levels was hampered by Dy^{3+} ions (reflected in the shortened lifetime of Yb^{3+}, Figure 2). Consequently, only a few Er^{3+} ions undergo efficient UC excitation followed by radiative decay, resulting in overall poor UC emission when Dy^{3+} ions are in proximity to the emitters. Growth of an outer $NaDyF_4$ shell resulted in even longer Er^{3+} lifetimes for both the green and red emissions (Figure S7A/B2/3), reaching lifetimes from ca. 240 to ca. 330 µs for ^{4nm}Dy-CSS^{3nm} and ^{6nm}Dy-CSS^{3nm} NPs, respectively, providing overall efficient protection from surface quenching. Figure S8 summarizes the interplay between the $Yb^{3+} \rightarrow Dy^{3+}$ energy transfer hampering efficient UC excitation of Er^{3+} and UC emission intensity as a function of NP architecture.

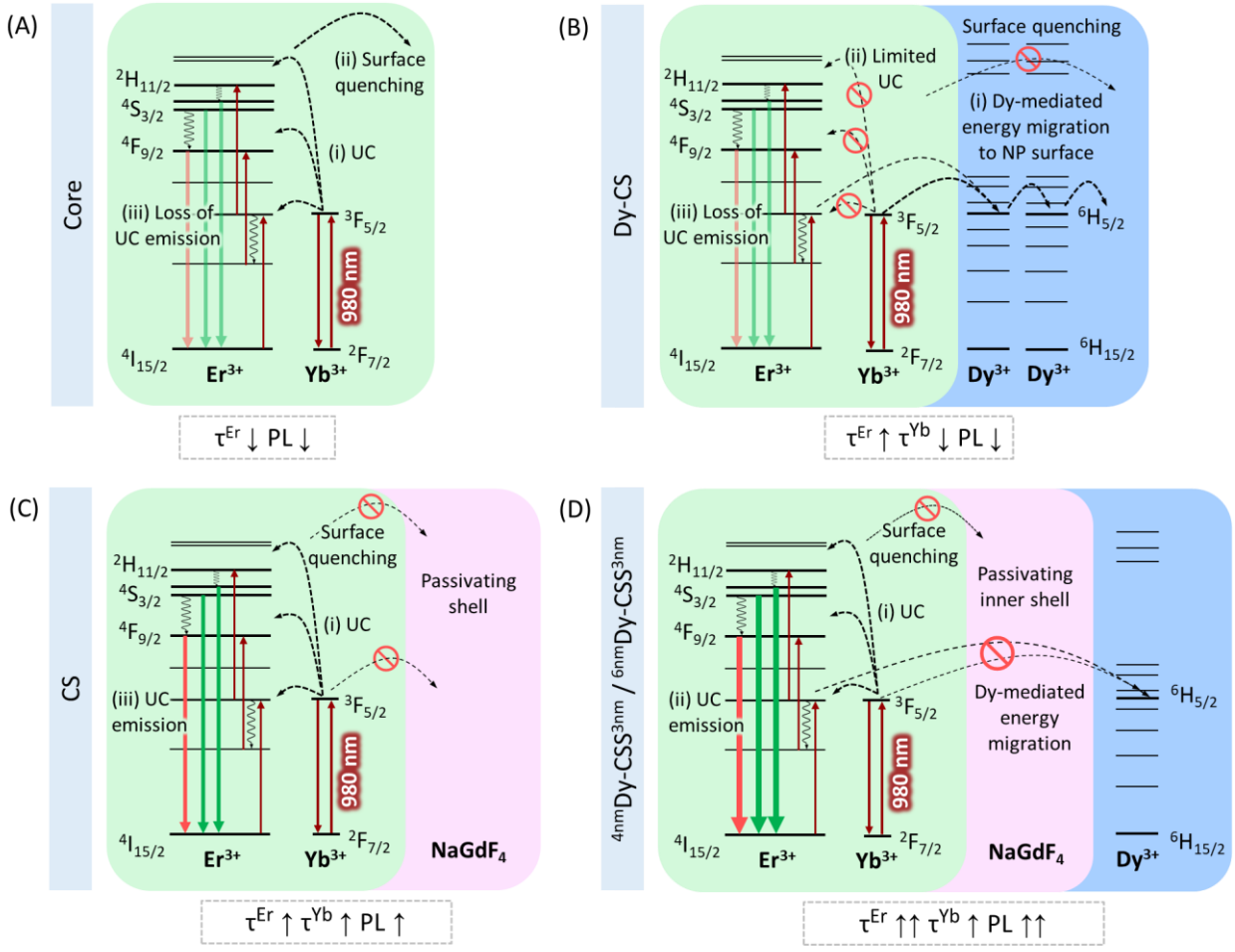

Figure S8. Partial energy level diagrams for UC pair Yb^{3+}/Er^{3+} and Dy^{3+} as well as mechanisms resulting in the observed architecture-dependent green and red UC emission intensities of (A) core, (B) Dy-CS, (C) CS, and (D) Dy-CSS NPs. The following dominating mechanisms are proposed based on UC emission intensities as well as Yb^{3+} and Er^{3+} excited state lifetimes: (A) Loss of UC emission due to surface quenching. (B) Loss of UC emission due to Dy^{3+}-mediated energy migration to the NP surface. (C) Enhancement of UC emission due to prevention of surface quenching. (D) Restoration and enhancement of UC emission due to prevention of Dy^{3+}-mediated energy migration and protection of the Er^{3+} excited states from surface quenching.

4. Additional Characterization of Dy-CSS NPs with Varying Outer Shell Thickness

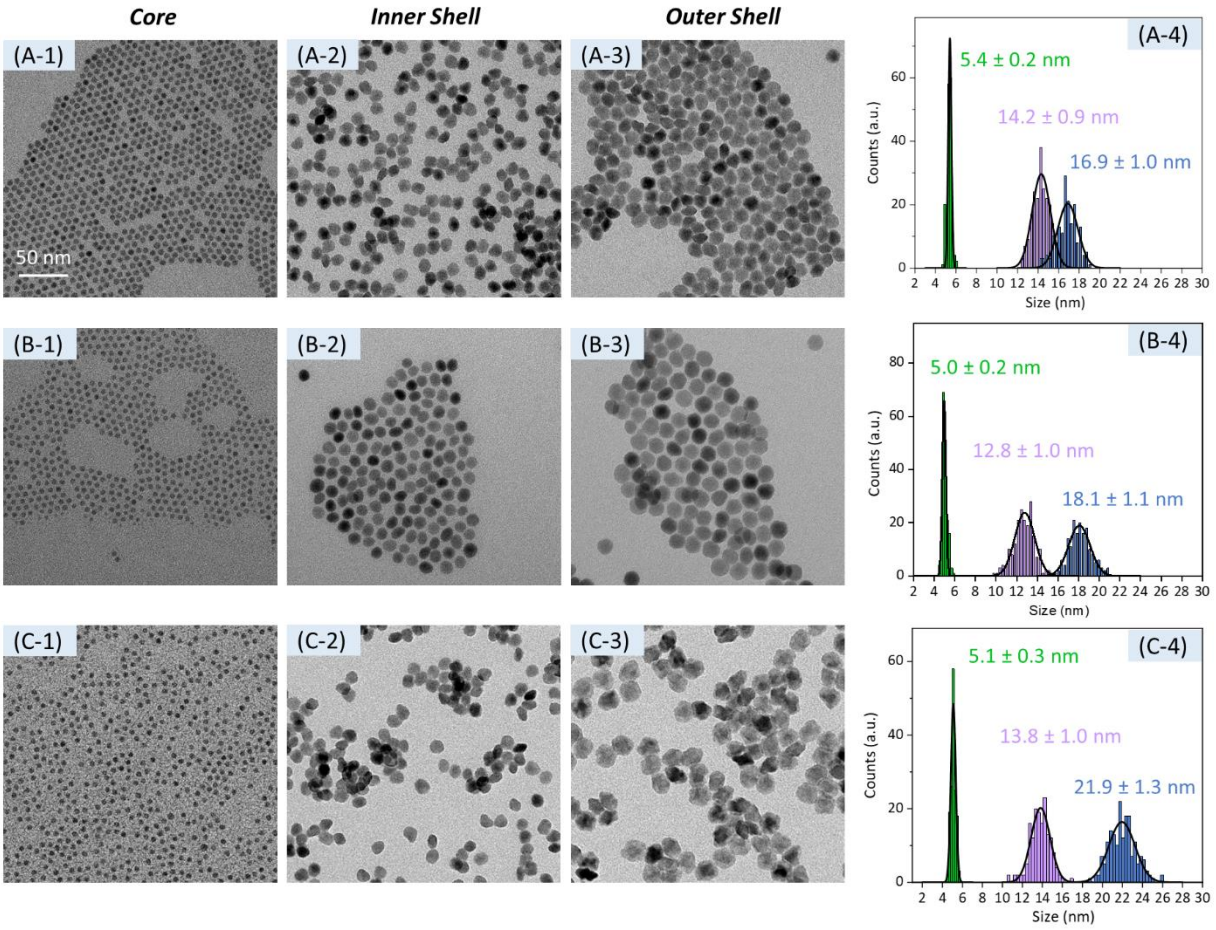

Figure S9. Dy-CSS NPs with tuned outer shell thickness: (1-3) TEM images and (4) their corresponding size distributions of OA-capped (A) ^{4nm}Dy-CSS^{1nm}, (B) ^{4nm}Dy-CSS^{3nm} and (C) ^{4nm}Dy-CSS^{4nm} NPs. The core diameter and the thickness of the inner shell were kept constant. The 50 nm scale bar applies to all TEM images.

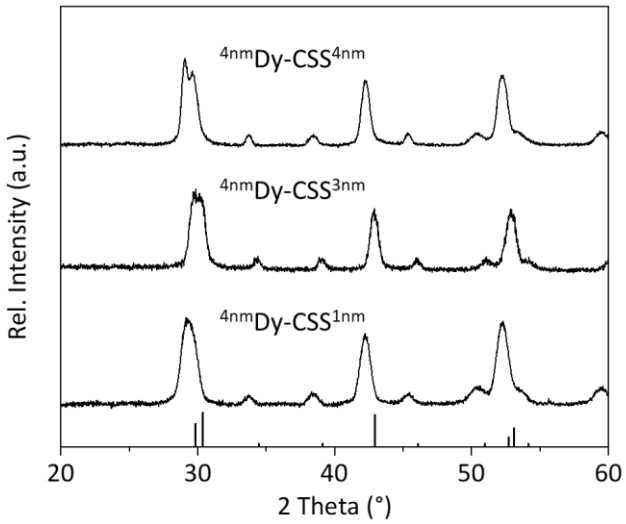

Figure S10. XRD patterns of OA-capped ^{4nm}Dy-CSS^{1nm}, ^{4nm}Dy-CSS^{3nm} and ^{4nm}Dy-CSS^{4nm} NPs with tunable outer shell thickness. Reference: β-$NaGdF_4$, PDF card [01-080-8787].

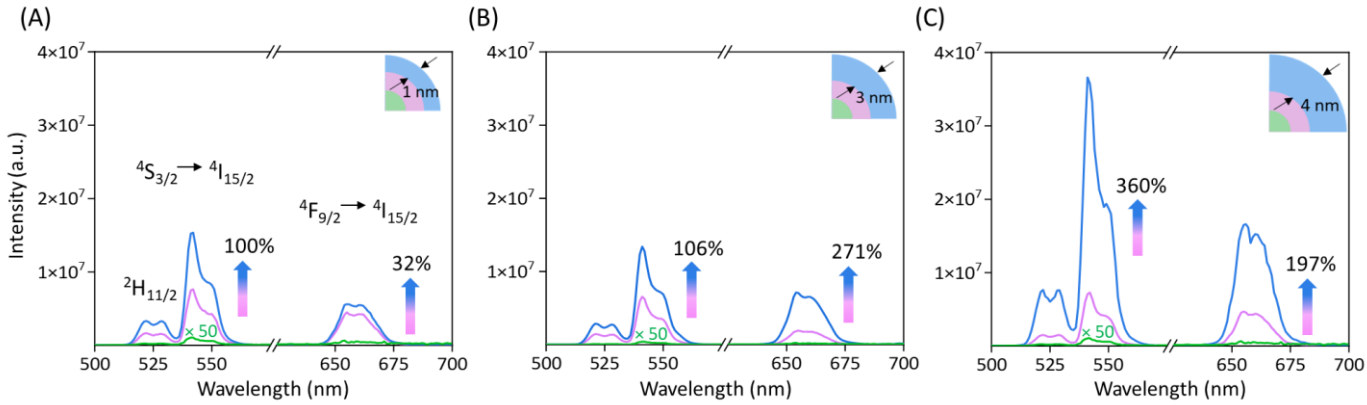

Figure S11. UC spectra of OA-capped (A) ^{4nm}Dy-CSS^{1nm}, (B) ^{4nm}Dy-CSS^{3nm} and (C) ^{4nm}Dy-CSS^{4nm} NPs (blue) as well as their corresponding core (green) and CS (pink) NPs. All spectra were obtained under 980 nm laser excitation. Power density = 6.0 W/cm^2, [NP] = 5 mg/mL in toluene.

Figure S11 shows the UC spectra of Dy-CSS NPs with comparable inner shell thickness (ca. 4 nm), yet, different outer shell thicknesses, 1 nm, 3 nm, and 4 nm, respectively. Due to the efficient inner shell protection, the emission intensities of Dy-CSS NPs in all the three samples were higher than those of their corresponding CS NPs. With the thinnest $NaDyF_4$ outer shell growth, the obtained ^{4nm}Dy-CSS^{1nm} NPs exhibited an enhancement of 100 % for the green and by ca. 32 % for the red emission compared to their respective ^{4nm}CS NPs (Figure S11A). The enhancement obtained between ^{4nm}Dy-CSS^{3nm} NPs and their corresponding ^{4nm}CS NPs (Figure S11B) was 106 % for the green and 271 % for the red emission, due to the thicker outer shell thickness. When the $NaDyF_4$ shell thickness increased to ca. 4 nm, the obtained ^{4nm}Dy-CSS^{4nm} NPs showed the strongest intensity among all the samples due to its overall thick shell ($NaGdF_4$ + $NaDyF_4$: 8.4 nm) (Figure S11C).

5. Characterization of Citrate-capped Dy-CSS NPs

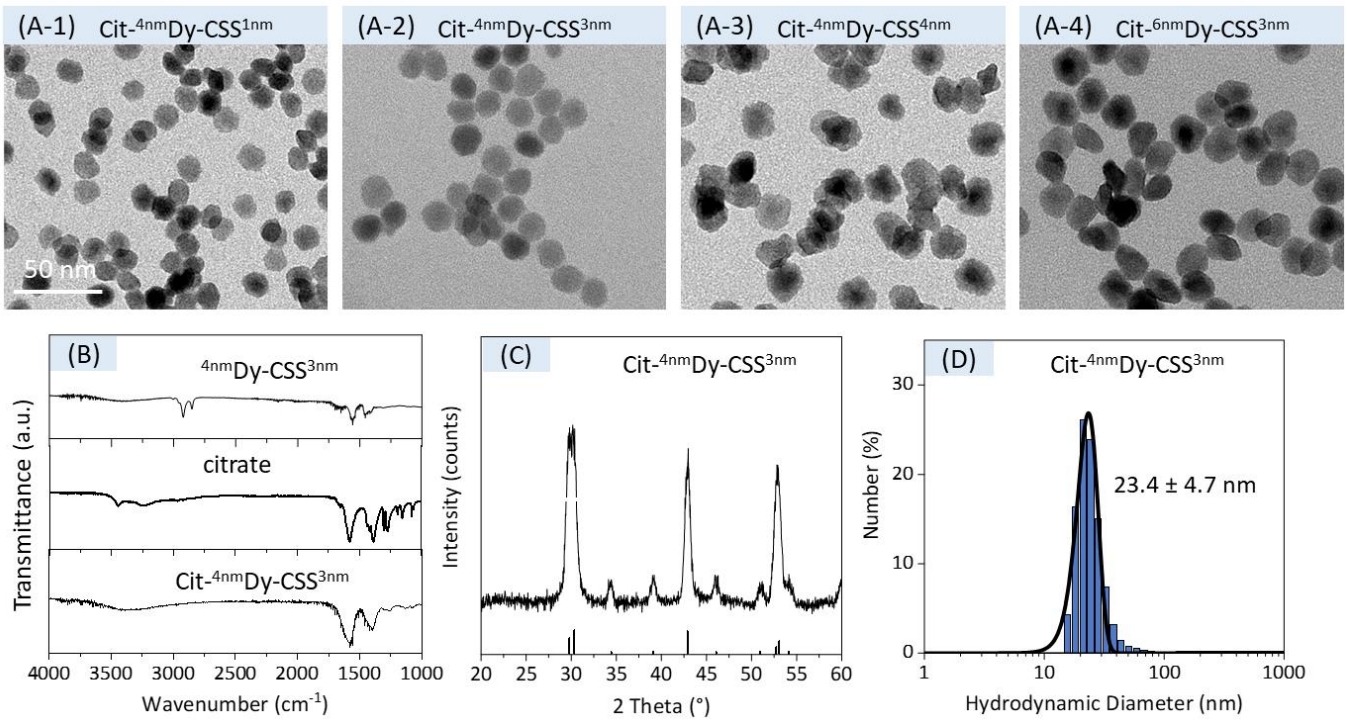

Figure S12. (A) TEM images of Cit-^{4nm}Dy-CSS^{1nm} (1), Cit-^{4nm}Dy-CSS^{3nm} (2), Cit-^{4nm}Dy-CSS^{4nm} (3) and Cit-^{6nm}Dy-CSS^{3nm}. The 50 nm scale bar applies to all TEM images. (B) FTIR spectra of citrate- and OA-capped ^{4nm}Dy-CSS^{3nm} NPs as well as citrate used as a reference. (C) XRD pattern of Cit-^{4nm}Dy-CSS^{3nm} NPs. Reference: β-$NaGdF_4$, PDF card [01-080-8787]. (D) DLS curve of Cit-^{4nm}Dy-CSS^{3nm} NPs dispersed in water. DLS data revealed a hydrodynamic diameter of 23.4 nm (PDI: 0.27).

To explore the capability of the obtained Dy-CSS NPs for biomedical applications, the NPs had to be rendered hydrophilic and water dispersible. Citrate (Cit) groups were chosen as a model capping agent to transfer the as-obtained, hydrophobic OA-capped NPs into water. The surface modification of OA-capped NPs with citrate groups was obtained through a ligand exchange process described in the Experimental Section. ^{3nm}Dy-CSS^{3nm} NPs were disregarded given their inferior optical performance. The morphology of the citrate-capped Dy-CSS NPs was confirmed by TEM analysis (Figure S12A), showing the same morphology and size comparing to their OA-capped counterparts. A representative Cit-^{4nm}Dy-CSS^{3nm} sample was selected for further characterization. As shown in Figure S12B, the successful citrate capping was confirmed by Fourier transform infrared (FTIR) spectroscopy. The crystallinity of the Cit-^{4nm}Dy-CSS^{3nm} NPs was confirmed by XRD analysis (Figure S12C), showing that the pure hexagonal phase was retained. The hydrodynamic diameter of the Cit-^{4nm}Dy-CSS^{3nm} NPs was determined to 23.4 ± 4.7 nm (PDI: 0.27) (Figure S12D), while the NPs exhibited a negative zeta potential of -32.4 ± 0.4 mV.

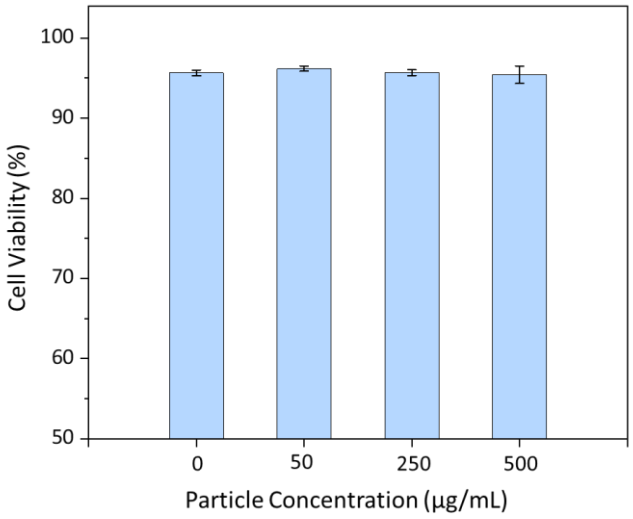

Figure S13. Cell viability of A549 cells incubated with Cit-^{4nm}Dy-CSS^{3nm} NPs at different concentrations (0, 50, 250, and 500 μg/mL) for 24 h at 37 °C.

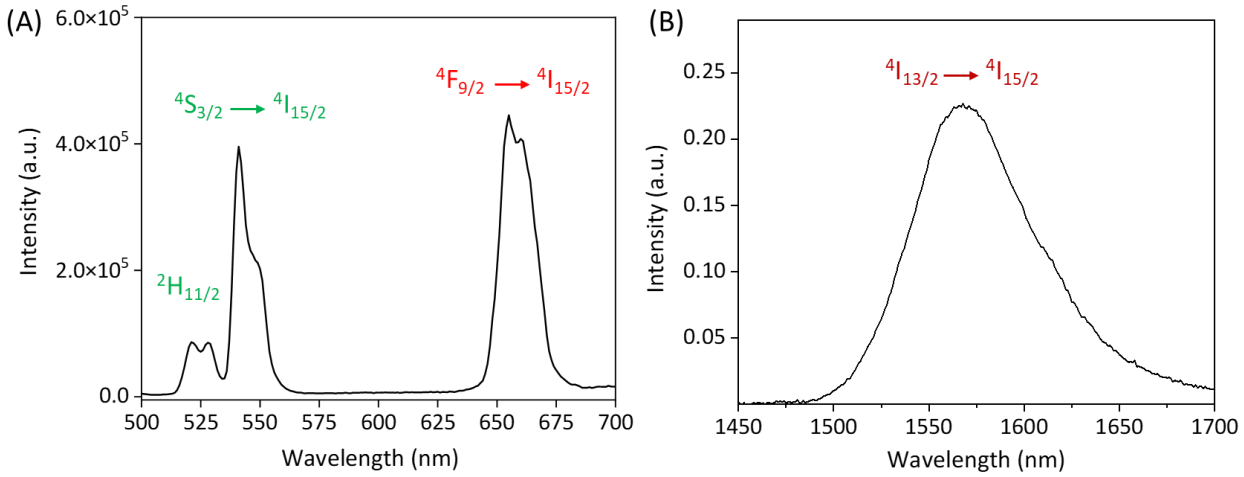

Figure S14. Upconversion (A) and downshifting (B) luminescence spectra of Cit-^{4nm}Dy-CSS^{3nm} NPs (5 mg/mL in water for UC emission, 10 mg/mL in water for NIR emission) obtained under 980 nm laser excitation. Power densities used to trigger upconversion and NIR emission were 6.0 W/cm^2 and 33.3 W/cm^2, respectively.

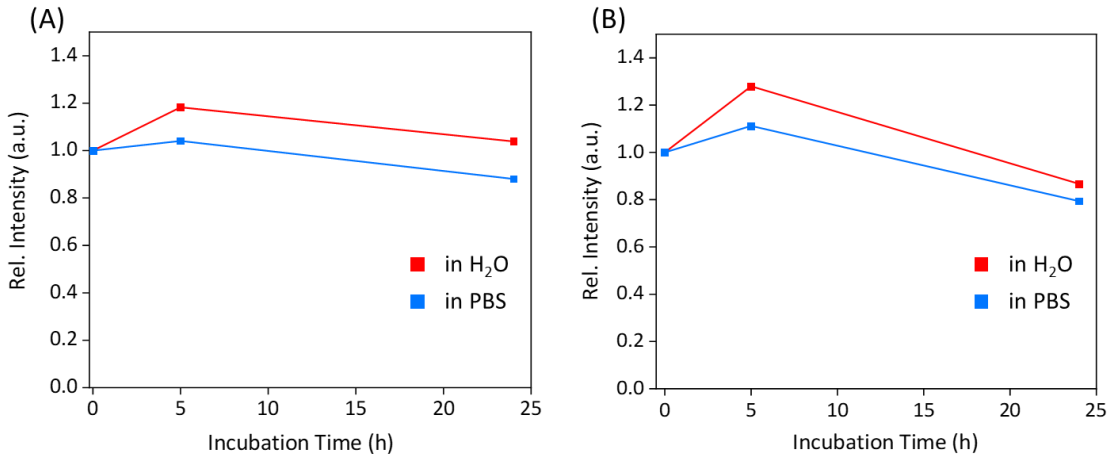

Figure S15. Overall upconversion emission intensity of Cit-^{4nm}Dy-CSS^{3nm} NPs as a function of incubation time in H_2O and phosphate-buffered saline (PBS) at (A) room temperature and (B) 37 °C.

The photoluminescence stability of Cit-^{4nm}Dy-CSS^{3nm} NPs was assessed by monitoring the Er^{3+} UC emission intensity of the NPs in water and PBS buffer, respectively, at room temperature and 37 °C as a function of time. As shown in Figure S15A, at room temperature, the UC emission intensity of Cit-^{4nm}Dy-CSS^{3nm} NPs in water remained after 24 h incubation, while a slight decrease of 10% was observed in PBS buffer. The emission intensities retained 80 % when incubating the NPs in water and PBS at 37°C after 24 h (Figure S15B).

6. Nanothermometry of Cit-Dy-CSS NPs

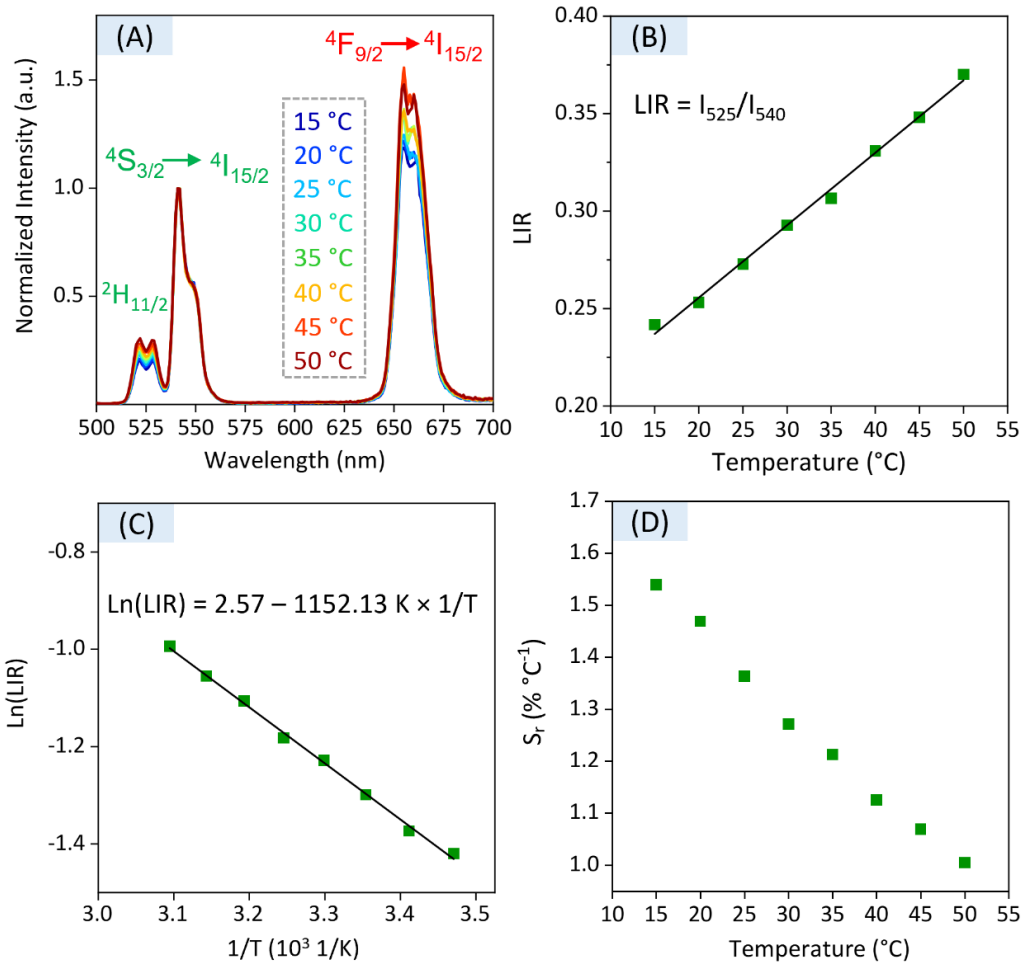

Figure S16. (A) Temperature-dependent emission spectra of Cit-^{4nm}Dy-CSS^{3nm} NPs dispersed in water. (B) Luminescence intensity ratio (LIR) between the two green emission bands stemming from the $^2H_{11/2}$ and $^4S_{3/2}$ excited levels plotted against temperature. (C) Natural logarithm of LIR plotted as a function of the inverse absolute temperature (Boltzmann's plot). (D) Relative thermal sensitivity, S_r, plotted as a function of the temperature.

Er^{3+}-based upconverting nanoparticles are well known for their thermometric sensing capabilities, whereas the temperature-induced change in luminescence intensity ratio (LIR) – LIR being the ratio between the $^2H_{11/2} \rightarrow {}^4I_{15/2}$ (525 nm) and $^4S_{3/2} \rightarrow {}^4I_{15/2}$ (540 nm) emission intensities – is a suitable and popular thermometric parameter.[6, 7] In order to assess the performance of Cit-^{4nm}Dy-CSS^{3nm} NPs dispersed in water as nanothermometers, temperature-dependent UC spectra were recorded from 15 to 50 °C, including the physiologically relevant range from 35 to 45 °C. As shown in Figure S16A, an increase of the emission intensity at 525 nm ($^2H_{11/2} \rightarrow {}^4I_{15/2}$) relative to that at 540 nm ($^4S_{3/2} \rightarrow {}^4I_{15/2}$) was observed upon temperature increase. This is expected as higher temperatures provide the energy required for the population of the higher laying $^2H_{11/2}$ Er^{3+} level.

The thermometric parameter, LIR = I_{525}/I_{540}, was calculated using the two integrated spectral regions of I_{525} (500 - 535 nm) and I_{540} (535 - 575 nm). The obtained LIR values as a function of temperature are shown in Figure S16B. The temperature governed population of the two closely spaced energy levels of Er^{3+} follows a Boltzmann's distribution, and LIR can be expressed by equation S1:

$$LIR = \frac{I_{525}}{I_{540}} = B \times \exp\left(-\frac{\Delta E}{k_B T}\right) \quad \text{(S1)}$$

where ΔE is the energy gap between the emitting levels in close proximity, I_{525} and I_{540}, and B is a constant that depends on the experimental system and the intrinsic spectroscopic parameters of the dopant/host pair. T is given in Kelvin. k_B is the Boltzmann factor. The Boltzmann's plot and its linear fits for Cit-^{4nm}Dy-CSS^{3nm} are shown in Figure S16C.

Based on the obtained Boltzmann's plots, the thermal sensitivity S as a function of the temperature can be determined by equation S2:

$$S = \frac{\partial LIR}{\partial T} = LIR \times \frac{\Delta E}{k_B T} \quad \text{(S2)}$$

To calculate the relative thermal sensitivity, S_r, which is commonly used as a figure of merit to compare the performance of different thermometers, the following expression was employed:

$$S_r = \frac{1}{LIR} \times \frac{\partial LIR}{\partial T} \quad \text{(S3)}$$

As shown in Figure S16D, the S_r values obtained for the Dy-CSS NPs were larger than 1% °C^{-1} over the assessed temperature range, with S_r values of ca. 1.1 to 1.2% °C^{-1} at physiologically relevant temperatures.

7. MRI T_1 Relaxivity Measurements

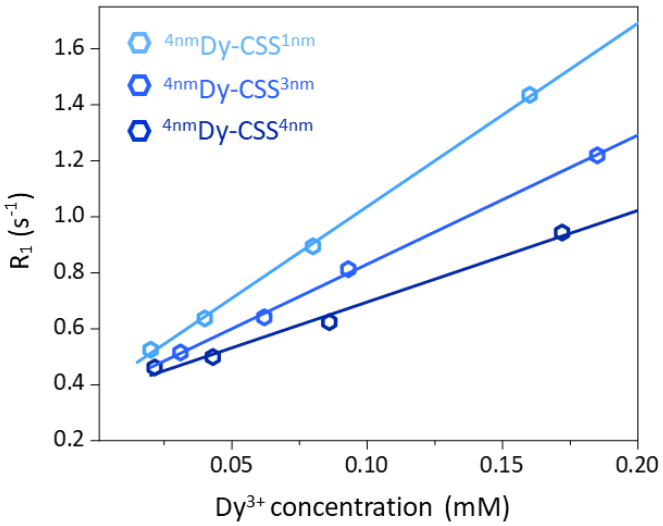

Figure S17. Relaxation rate R_1 (= $1/T_1$) of water protons plotted against the molar concentration of Dy^{3+} for Cit-^{4nm}Dy-CSS^{1nm}, Cit-^{4nm}Dy-CSS^{3nm} and Cit-^{4nm}Dy-CSS^{4nm} NPs at 7 T. The solid lines are linear fits.

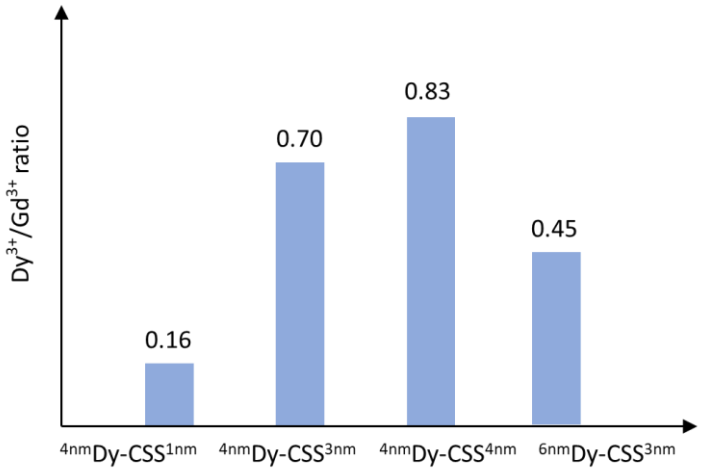

Figure S18. Dy^{3+}-to-Gd^{3+} ion ratio in the Dy-CSS NPs obtained from ICP measurements.

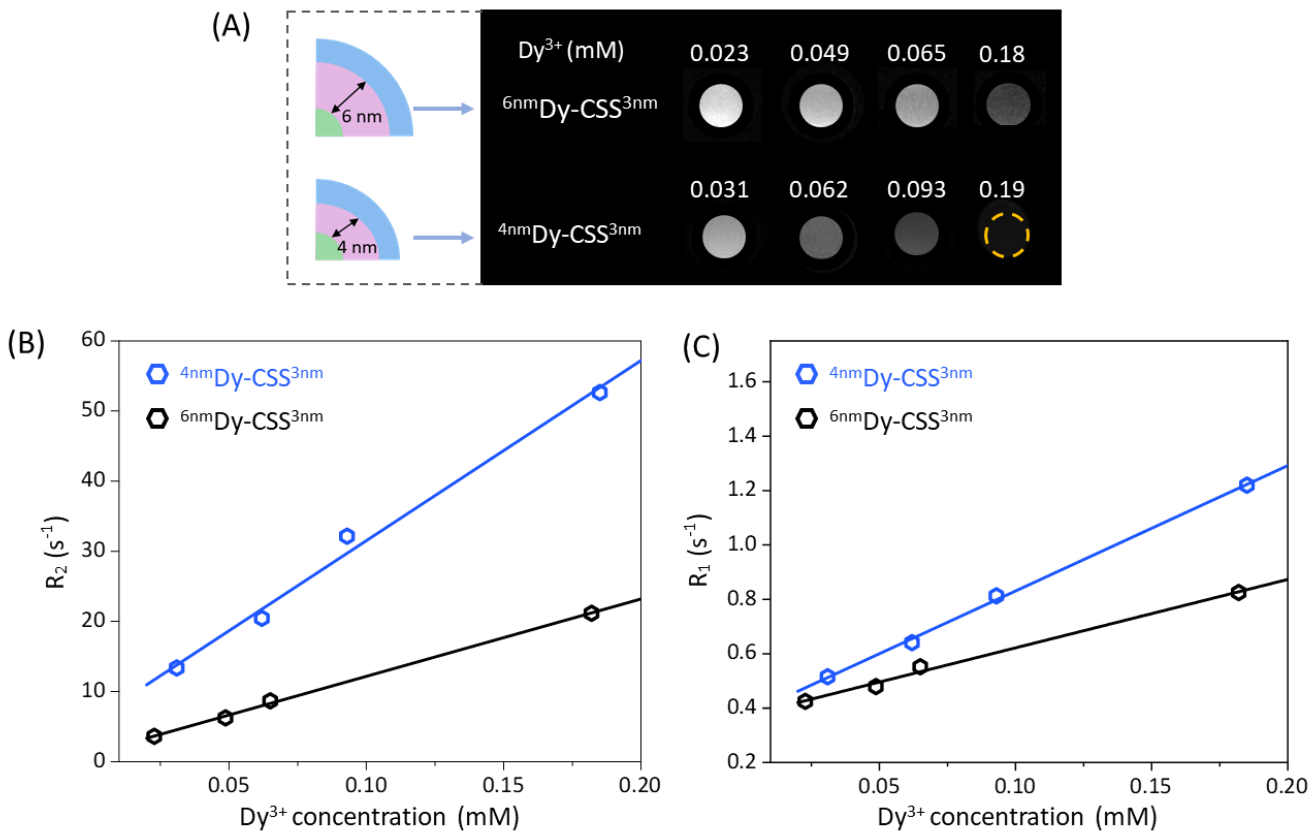

Figure S19. (A) T_2-weighted MR images of Cit-Dy-CSS NPs with varying $NaGdF_4$ inner shell thickness (Cit-^{4nm}Dy-CSS^{3nm} and Cit-^{6nm}Dy-CSS^{3nm}) as a function of the Dy^{3+} concentration. (B) Relaxation rate R_2 (= $1/T_2$) and (C) R_1 (=$1/T_1$) of water protons plotted against the molar concentration of Dy^{3+} for Cit-^{6nm}Dy-CSS^{3nm} and Cit-^{4nm}Dy-CSS^{3nm} at 7 T. Solid lines are linear fits.

Table S2. Comparison of MRI T_2 relaxivity values of clinically used iron oxide NPs, Dy-based chelates, and Dy-based NPs. The table also shows examples for multimodal CAs for additional optical and CT imaging.

Contrast Agents	Size (nm)	Surface Coating	r_2 (mM^{-1} s^{-1})	r_1 (mM^{-1} s^{-1})	r_2/r_1	Magnetic Field (T)	Other Imaging Capabilities	Ref.
Clinically used CAs								
Combidex (Fe_3O_4)	5.9	dextran	60.0	10	6.0	1.5		8
Feridex (Fe_3O_4, γ-Fe_2O_3)	5.0	dextran	93.0	4.1	22.7	3	-	9
Resovist (Fe_3O_4)	4.0	carboxy-dextran	146.0	4.6	31.7	3		9
Dy-based Chelates								
Dy-DOTA	-	-	20.0	-	-	9.4	-	10
Dy-DTPA-PcHexPh$_2$			3.0	0.1	30	7		11
Dy-based Nanoparticles								
$NaDyF_4$:Tb	30 × 35	CTAB[a]	22.3	-	-	7	optical	12
$NaDyF_4$	20.3	PMAO-PEG[b]	101.0	-	-	9.4	-	13
$NaGdF_4$:Dy	7.5	PEG[c]	10.6	5.2	2.0	9.4	CT	14
$NaGdF_4$:Yb,Er /$NaYbF_4$:Dy(38 %)	31.0	citrate	70.0	0.5	140	9.4	optical	15
$NaLuF_4$:Yb,Tm /$NaLuF_4$/$NaDyF_4$	21 × 39	PC[d]	40.0	-	-	7	optical CT	16
$NaYbF_4$:Tm /CaF_2/$NaDyF_4$	16.0	citrate	41.0	-	-	7	optical CT	17
$NaYF_4$:Nd /$NaDyF_4$	15.7	liposome	44.0	-	-	11.7	optical	18
Dy_2O_3	70.0	dextran	190	-	-	7	-	19
Dy-doped γ-Fe_2O_3	4.2	PEG	123.3	-	-	1.5	-	20
Cit-^{4nm}Dy-CSS^{1nm}	16.9	citrate	260.0	6.5	40.0	7	optical CT	this work
Cit-^{4nm}Dy-CSS^{3nm}	18.1	citrate	256.9	4.6	55.8	7	optical CT	this work
Cit-^{4nm}Dy-CSS^{4nm}	21.9	citrate	442.1	3.3	134	7	optical CT	this work
Cit-^{6nm}Dy-CSS^{3nm}	22.0	citrate	116.0	2.5	46.4	7	optical	this work

[a]CTAB: cetyl trimethyl ammonium bromide, [b]PMAO-PEG: poly(maleic anhydride-alt-1-octadecene) (PMAO) with polyethylene glycol (PEG), [c]PEG: polyethylene glycol, [d]PC: phosphatidylcholines.

8. X-ray Spectroscopy and Radiography Imaging Measurements

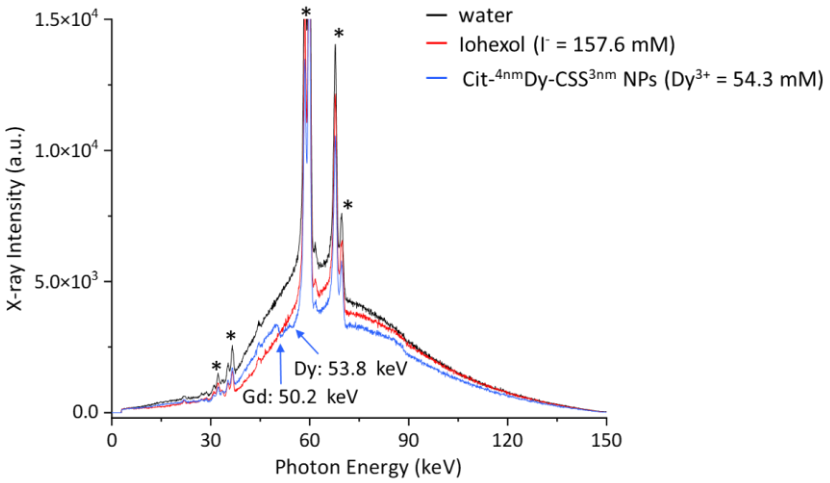

Figure S20. X-ray absorption spectra for water, Iohexol, and Cit-^{4nm}Dy-CSS^{3nm} NPs using a tungsten X-ray tube operating at 150 kV. Peaks marked with stars belong to the X-ray source, tungsten.

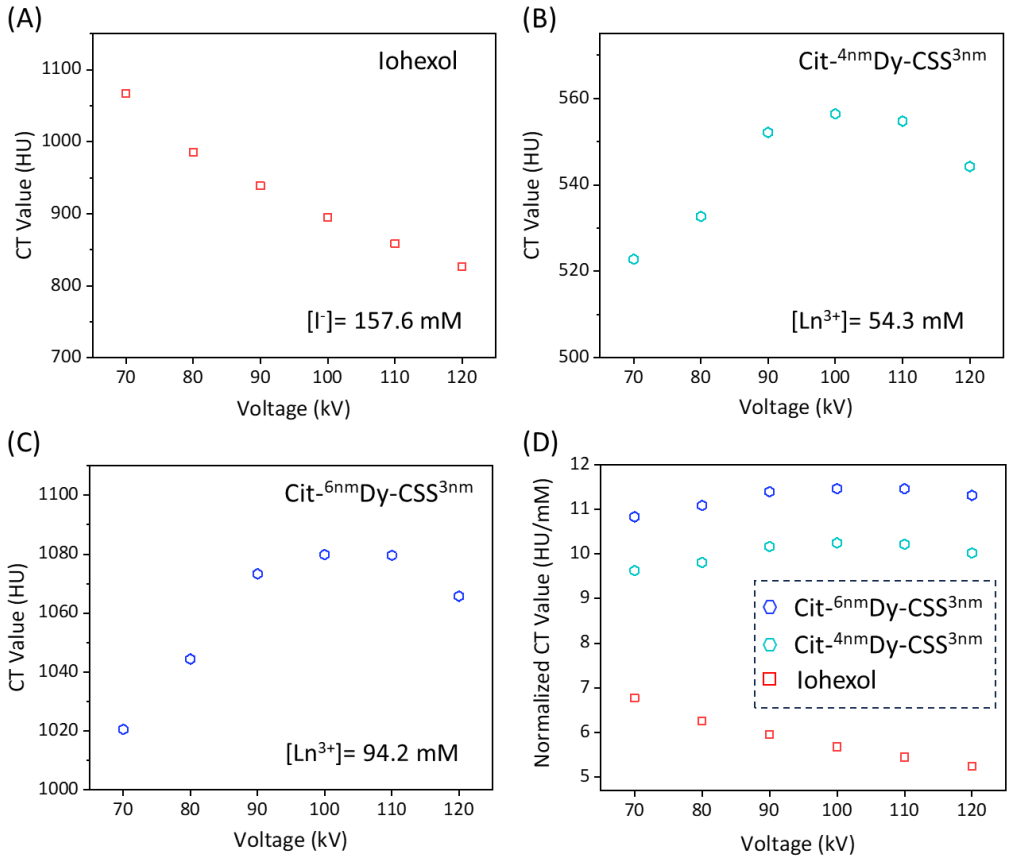

Figure S21. CT values of (A) Iohexol, (B) Cit-^{4nm}Dy-CSS^{3nm} NPs, (C) Cit-^{6nm}Dy-CSS^{3nm} NPs, and (D) their corresponding normalized values as a function of X-ray source peak voltage.

References

1. I. Halimi, E. M. Rodrigues, S. L. Maurizio, H.-Q. T. Sun, M. Grewal, E. M. Boase, N. Liu, R. Marin and E. Hemmer, *J. Mater. Chem. C*, 2019, **7**, 15364-15374.
2. N. J. J. Johnson and F. C. J. M. van Veggel, *Nano Research*, 2013, **6**, 547-561.
3. N. Liu, N. Gobeil, P. Evers, I. Gessner, E. M. Rodrigues and E. Hemmer, *Dalton Trans.*, 2020, **49**, 16204-16216.
4. A. Schroter, S. Märkl, N. Weitzel and T. Hirsch, *Adv. Funct. Mater.*, 2022, **32**, 2113065.
5. J. Bergstrand, Q. Liu, B. Huang, X. Peng, C. Wurth, U. Resch-Genger, Q. Zhan, J. Widengren, H. Agren and H. Liu, *Nanoscale*, 2019, **11**, 4959-4969.
6. A. Bednarkiewicz, L. Marciniak, L. D. Carlos and D. Jaque, *Nanoscale*, 2020, **12**, 14405-14421.
7. D. Jaque and F. Vetrone, *Nanoscale*, 2012, **4**, 4301-4326.
8. Y. X. Wang, *Quant. Imaging Med. Surg.*, 2011, **1**, 35-40.
9. H. B. Martin Rohrer, Jan Mintorovitch, P Martin Requardt and H.-J. Weinmann, *Invest. Radiol.*, 2005, **40**, 715-724.
10. M. Harris, L. Vander Elst, S. Laurent and T. N. Parac-Vogt, *Dalton Trans.*, 2016, **45**, 4791-4801.
11. P. Caravan, M. T. Greenfield and J. W. Bulte, *Magn. Reson. Med.*, 2001, **46**, 917-922.
12. Y. Zhang, V. Vijayaragavan, G. K. Das, K. K. Bhakoo and T. T. Y. Tan, *Eur. J. Inorg. Chem.*, 2012, **2012**, 2044-2048.
13. G. K. Das, N. J. Johnson, J. Cramen, B. Blasiak, P. Latta, B. Tomanek and F. C. van Veggel, *J. Phys. Chem. Lett.*, 2012, **3**, 524-529.
14. X. Jin, F. Fang, J. Liu, C. Jiang, X. Han, Z. Song, J. Chen, G. Sun, H. Lei and L. Lu, *Nanoscale*, 2015, **7**, 15680-15688.
15. S. Biju, M. Harris, L. V. Elst, M. Wolberg, C. Kirschhock and T. N. Parac-Vogt, *RSC Adv.*, 2016, **6**, 61443-61448.
16. W. Yuan, D. Yang, Q. Su, X. Zhu, T. Cao, Y. Sun, Y. Dai, W. Feng and F. Li, *Adv. Funct. Mater.*, 2016, **26**, 8631-8642.
17. Y. Li, Y. Gu, W. Yuan, T. Cao, K. Li, S. Yang, Z. Zhou and F. Li, *ACS Appl. Mater. Interfaces*, 2016, **8**, 19208-19216.
18. J. Zhao, H. Hu, W. Liu and X. Wang, *Nanoscale Adv.*, 2021, **3**, 463-470.
19. E. K. Małgorzata Norek, Uli Zeitler and J. A. Peters, *J. Am. Chem. Soc.*, 2008, **130**, 5335-5340.
20. J. Yin, F. Xu, H. Qu, C. Li, S. Liu, L. Liu and Y. Shao, *Phys. Chem. Chem. Phys.*, 2019, **21**, 11883-11891.